RSC Sustainability

ROYAL SOCIETY OF CHEMISTRY

PAPER

View Article Online
View Journal



Cite this: DOI: 10.1039/d5su00783f

# Catalytic aerobic oxidation of 5-hydroxymethylfurfural to 2,5-furandicarboxylic acid using Co–Mn/N–C catalysts in aqueous media

Shuolin Zhou, *[a] Sha Wen,[b] Ying Liu[a] and Xianxiang Liu *[b]

Received 5th October 2025
Accepted 25th March 2026

DOI: 10.1039/d5su00783f

rsc.li/rscsus

Aerobic oxidation of 5-hydroxymethylfurfural (HMF) can yield numerous furan-based chemicals, and enhancing the selectivity for specific products poses a significant challenge. In this study, a novel non-noble bimetallic catalyst supported on N-doped carbon (Co–Mn/N–C) was designed and synthesized, and various characterization techniques, including XRD, BET analysis, TEM, XPS and VSM studies, were employed to investigate the catalyst's structure and properties. Catalytic testing studies demonstrated that Co–Mn/N–C exhibits superior catalytic performance in the selective oxidation of HMF to 2,5-furandicarboxylic acid (FDCA) in aqueous media, outperforming both Co/N–C and Mn/N–C catalysts. Nearly 100% HMF conversion and 98.3% selectivity towards FDCA were achieved using the Co–Mn/N–C catalyst at 150 °C with $Na_2CO_3$ (0.5 mmol) as a base. Furthermore, the Co–Mn/N–C catalyst exhibited good stability, maintaining its catalytic activity throughout the recycling experiments. This stable performance is attributed to the robust interaction between the metal and nitrogen-carbon materials.

**Sustainability spotlight**

As humanity's rapid development continues, the once-abundant reserves of fossil resources are steadily dwindling, intensifying concerns over the long-term sustainability of energy and raw material supplies. In this study, the oxidation of 5-hydroxymethylfurfural (HMF) to furan-based chemicals was achieved under an $O_2$ atmosphere in water using Co–Mn/N–C catalysts. This approach offers a promising strategy for developing non-precious-metal catalytic processes under mild conditions. The findings presented here are expected to significantly advance the field of biomass conversion, aligning with the United Nations Sustainable Development Goals 12 (responsible consumption and production).

## 1 Introduction

As human society continues its rapid development, the once-plentiful reserves of fossil resources are gradually diminishing, thereby raising a pressing concern for the sustainable future of energy and raw material supplies.[1] The continuing decline in the supply of fossil resources highlights the urgent need to explore alternative resources to meet the growing needs of an evolving human civilization.[2] Biomass resources, the most abundant renewable resource on the earth, have garnered significant attention from the perspective of scientific research and industrial applications.[3–6] Among the biomass-based platform chemicals, 5-hydroxymethylfurfural (HMF) can be further converted into a series of various fine chemicals with promising application prospects *via* esterification,[7,8] hydrogenation[9–12] and oxidation.[13–22] As shown in Scheme 1, there are several industrially valuable furan compounds such as 2,5-diformylfuran (DFF), 5-formyl-2-furancarboxylic acid (FFCA), 5-hydroxymethyl-2-furancarboxylic acid (HFCA) and 2,5-furandicarboxylic acid (FDCA), which are oxidized from HMF.[15,23–28] As an oxidation product of HMF, FDCA possesses two carboxylic acid groups, making it akin to terephthalic acid (TPA). In addition, FDCA can be utilized in the production of polyethylene furanoate (PEF) polymers, a bio-based polymer that can serve as a sustainable alternative to polyethylene terephthalate (PET).[29,30] Besides, FDCA, as a promising furan chemical, can be further used for synthesizing various derivatives such as succinic acid, 2,5-dihydroxymethylfuran, 2,5-dihydroxymethyl tetrahydrofuran, and 2,5-furandicarbaldehyde.[31] Considering the promising potential of FDCA, numerous endeavors have been undertaken to devise effective chemocatalytic approaches to efficiently convert HMF into FDCA.[32] Due to the variability in oxidation products resulting from variations in the degree of HMF oxidation, achieving high selectivity in the production of FDCA remains a formidable challenge for most researchers.[33,34]

In recent years, there have been many studies focusing on the development of non-noble metal catalysts for the catalytic

[a]*Changsha Normal University, Changsha 410100, China. E-mail: slzhou@csnu.edu.cn*
[b]*National & Local Joint Engineering Laboratory for New Petro-chemical Materials and Fine Utilization of Resources, Key Laboratory of the Assembly and Application of Organic Functional Molecules of Hunan Province, Hunan Normal University, Changsha 410081, China. E-mail: lxx@hunnu.edu.cn*

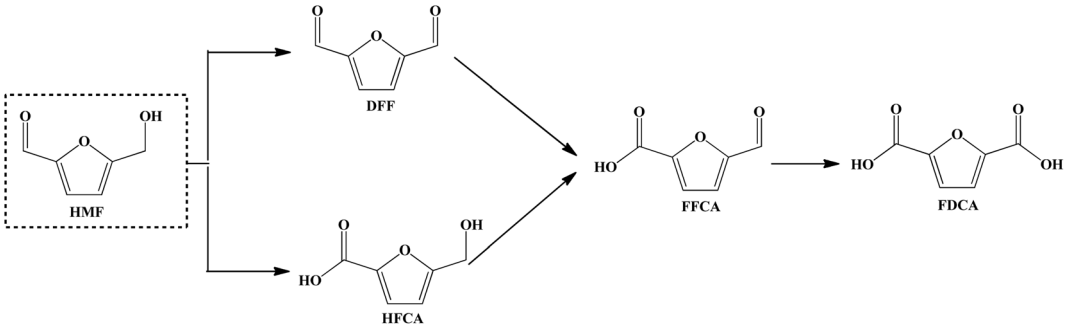


Scheme 1 Reaction pathways for HMF oxidation.

oxidation of HMF to produce FDCA.[16,35–37] Transition metals typically exhibit tunable pH adaptability, redox capabilities, crystal defects, and diverse oxygen species. This is attributed to the variable three-dimensional electron orbital configurations of transition metals. These characteristics can effectively improve the selectivity of desired products of the oxidation reaction.[38] Transition metals such as manganese (Mn), cobalt (Co), and iron (Fe) were investigated as promising candidates for the catalytic oxidation of HMF. This may be motivated by the desire to harness the unique properties of these metals for targeted oxidation processes.[39,40] For example, Han *et al.* prepared a $MnO_x$-$CeO_2$ bimetal oxide catalyst and applied it in the aerobic oxidation of HMF to prepare FDCA, and the yield of FDCA was as high as 91.0%, and the catalyst could be reused 5 times.[41] Lu *et al.* introduced $Fe_3O_4$ into α-$MnO_2$ to form complex metal oxides, and studied the oxidation behavior of these Mn–Fe oxides catalyzing HMF. Among them, $Mn_8Fe_3O_x$ showed the best catalytic performance for HMF oxidation to synthesize FDCA.[42] Under the optimal conditions, HMF can be completely transformed, and the yield of FDCA was 76.9%. Yang *et al.* synthesized nano-spherical mesoporous silica (NS-MS) with modification by bimetal (Co–Mn) oxides *via* a modified micelle template method.[43] The HMF conversion rate was close to 100%, and the yield of FDCA was up to 72.4%. Despite the significant progress made in the utilization of non-precious metal catalysts for the oxidation of HMF, the quest for achieving high selectivity towards the desired products under conditions that are both mild and environmentally benign remains a challenge that necessitates further research and development.[44]

Based on our recent work toward oxidation catalysts for HMF conversion,[45–47] we herein synthesize a novel rod-like magnetic Co–Mn/N–C bimetal supported on N-doped carbon, using citric acid, melamine, $MnSO_4$ and $CoCl_2$ as precursors. Characterization techniques, including XRD, nitrogen adsorption–desorption studies, XPS, and TEM, were employed to analyze the structure of the catalyst. As expected, the Co–Mn/N–C catalyst was successfully obtained. The catalytic performance of this catalyst in the oxidation process for the production of FDCA from HMF in water was evaluated. In addition, the effect of various reaction parameters on the oxidation of HMF was investigated. A HMF conversion of nearly 100% with an FDCA selectivity of 98.3% was achieved under optimal conditions.

## 2 Experimental section

### 2.1 Chemicals

5-Hydroxymethylfurfural (97.0%), 2,5-furandicarboxylic acid (98.0%), $CoCl_2 \cdot 6H_2O$ (≥99.0%) and melamine (≥99.0%) were purchased from Shanghai Macklin Biochemical Co., Ltd (Shanghai, China). Citric Acid (≥99.5%), $MnSO_4 \cdot H_2O$ (≥99.0%), $NaHCO_3$ (≥99.5%) and $Na_2CO_3$ (≥99.8%) were obtained from Sinopharm Group Co., Ltd (Shanghai, China).

### 2.2 Synthesis of Co–Mn/N–C

The catalysts were prepared according to the procedure presented in Scheme 2. Citric acid primarily acts as a chelating agent to coordinate with $Co^{2+}$ and $Mn^{2+}$ ions, and melamine is employed as a nitrogen-rich precursor for the N-doped carbon support. Firstly, $CoCl_2 \cdot 6H_2O$, $MnSO_4 \cdot H_2O$, citric acid and melamine were dissolved in deionized water at 100 °C for 3 h. Subsequently, the mixture was washed and filtered, followed by drying in an oven at 100 °C. The resulting sample was calcined at 700 °C for 3 h, yielding the product denoted as Co–Mn/N–C.

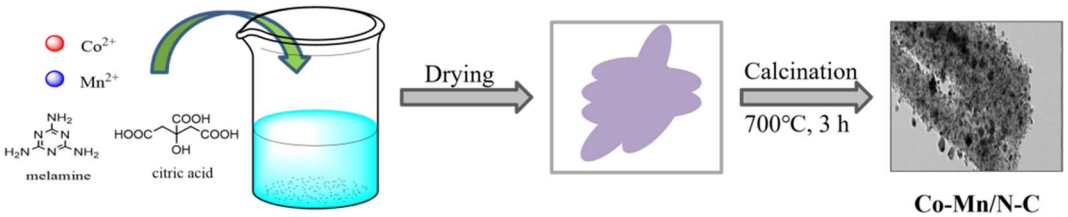


Scheme 2 Schematic of the synthesis steps for the Co–Mn/N–C catalyst.

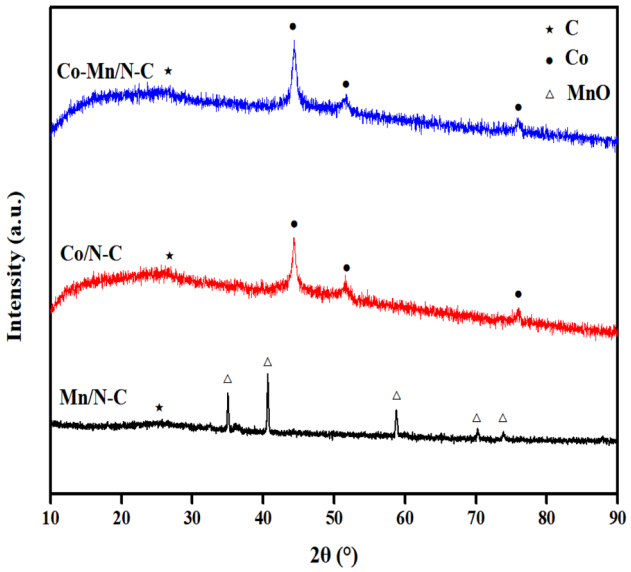


Fig. 1 XRD spectra of Co–Mn/N–C, Co/N–C, and Mn/N–C.

Under identical operational conditions, Co/N–C and Mn/N–C were synthesized. The Co/N–C catalyst was derived from a precursor mixture comprising $CoCl_2 \cdot 6H_2O$, citric acid, and melamine. Similarly, the Mn/N–C catalyst was prepared from a precursor mixture comprising $MnSO_4 \cdot H_2O$, citric acid, and melamine.

### 2.3 Characterizations techniques

The catalyst morphology was characterized by transmission electron microscopy (TEM, JEM 2100F). Thermogravimetry-differential thermal analysis (TG-DTG, Germany) curves were recorded in an $N_2$ flow on a Netzsch Model STA 409 PC instrument using $\alpha$-$Al_2O_3$ as the standard material. Data were recorded at a temperature range from room temperature to 800 °C with a heating rate of 10 °C $min^{-1}$. X-ray diffraction (XRD) studies were carried out using a Bruker diffractometer with Cu K$\alpha$ radiation to survey the crystal structure and diffraction angles ($2\theta$) ranging from 10° to 80°. The magnetic properties were probed using a Lake Shore superconducting vibrating sample magnetometer (VSM). XPS was conducted using a Thermo Scientific K-Alpha$^+$ spectrometer, and the XPS Peak 4.1 software was utilized to fit the curves using the Shirley-type background subtraction.

### 2.4 HMF oxidation reaction

The catalytic oxidation reaction of HMF was carried out according to the following procedure: HMF (0.5 mmol) was dissolved in 10 mL of water, while the catalyst (20 mg) and $Na_2CO_3$ (0.5 mmol) were added. At 5 bar $O_2$ pressure, the reaction was

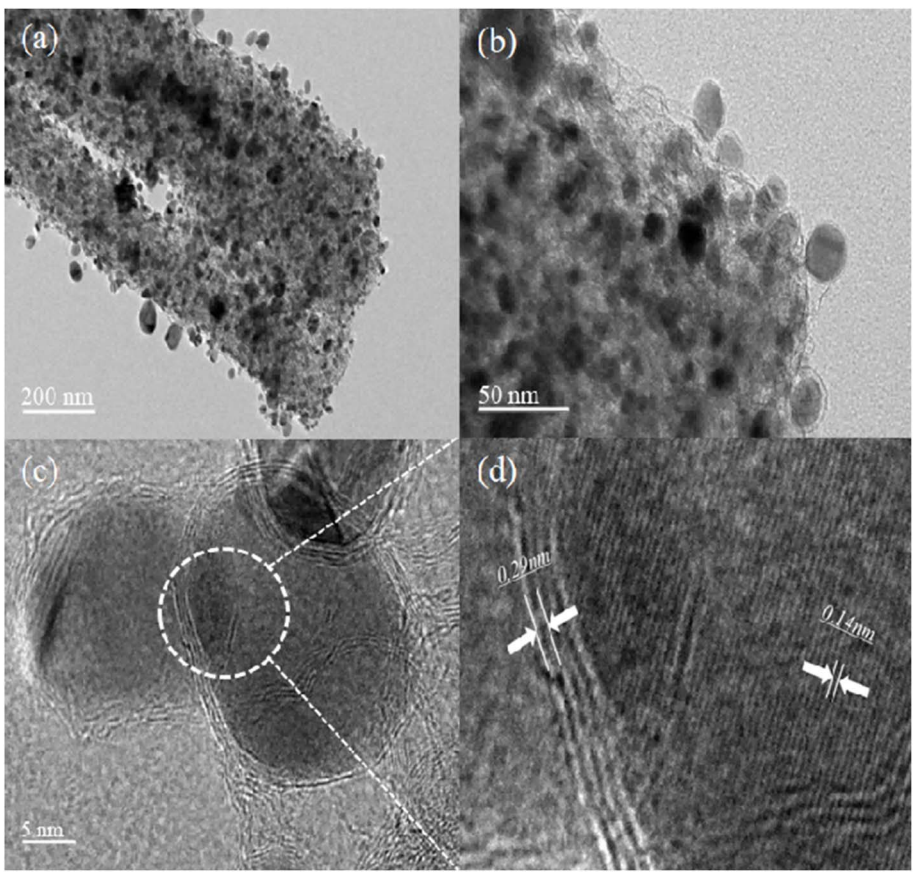


Fig. 2 HRTEM images of Co–Mn/N–C at different resolutions of (a) 200 nm, (b) 50 nm, and (c) 5 nm and (d) the corresponding zoomed-in area.

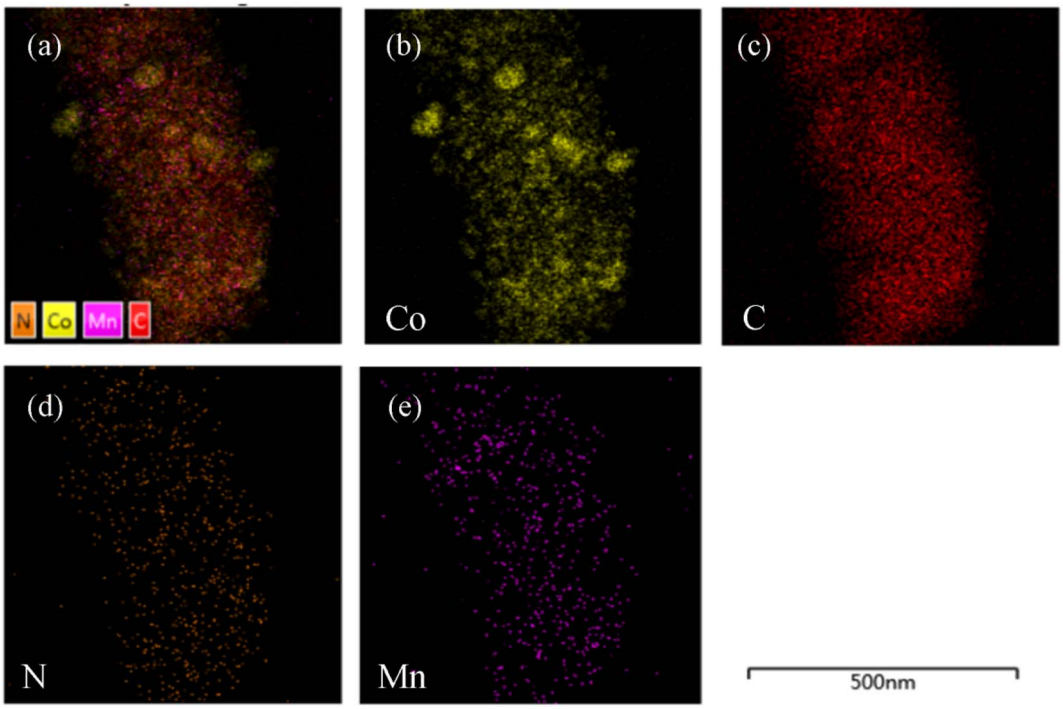


Fig. 3 Elemental mappings of Co–Mn/N–C: (a) overall, (b) Co, (c) C, (d) N and (e) Mn.

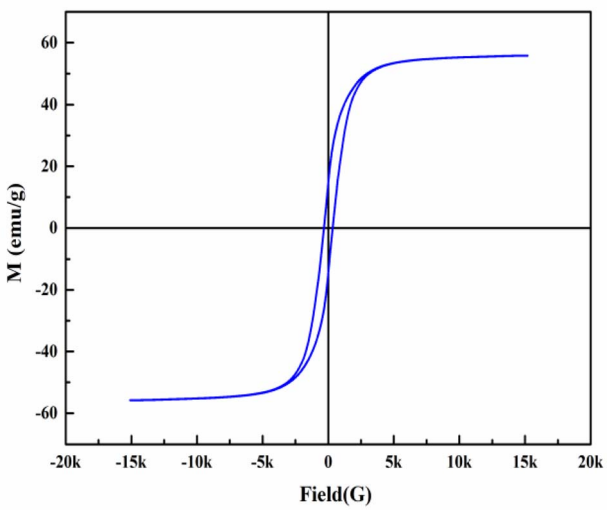


Fig. 4 VSM curve of Co–Mn/N–C.

carried out at 100 °C for 6 h in an autoclave with a Teflon liner. After the reaction, the reactor was cooled to room temperature. The reaction mixture was further analyzed using an Agilent 1260 HPLC system equipped with a Venusil XBP C18 chromatographic column (4.6 × 250 mm, 5 μm, Phenomenex, USA) and a UV-Vis (280 nm) detector. Quantification was carried out using the external standard method. The mobile phase consisted of an acetic acid solution (0.1 wt%) and acetonitrile with a volume ratio of 95 : 5, and the samples were eluted at a flow rate of 0.7 mL $min^{-1}$ at 30 °C. Typical HPLC results and $^1H$ NMR analysis for HMF oxidation products are shown in Fig. S1 and S2 in the SI. The HMF conversion and the selectivity of the main products were calculated using the following equations:

$$\text{HMF conversion} = (1 - \text{moles of HMF/added moles of HMF}) \times 100\%$$

$$\text{FDCA selectivity} = \text{moles of FDCA/(added moles of HMF} - \text{moles of HMF)} \times 100\%$$

$$\text{HFCA selectivity} = \text{moles of HFCA/(added moles of HMF} - \text{moles of HMF)} \times 100\%$$

$$\text{FFCA selectivity} = \text{moles of FFCA/(added moles of HMF} - \text{moles of HMF)} \times 100\%$$

# 3 Results and discussion

## 3.1 Catalyst characterization

The X-ray diffraction (XRD) spectra of Co–Mn/N–C, Mn/N–C, and Co/N–C are shown in Fig. 1. Co–Mn/N–C, Co/N–C, and Mn/N–C showed a wide peak centered at a $2\theta$ value of 26°, which was attributed to the (002) reflection plane graphitic carbon (JCPDS 41-1487).[48] In Fig. 1, the peaks at about 44.2°, 51.5° and 75.9° correspond to the (111), (200) and (220) lattice planes, respectively, of the cubic Co phase (JCPDS 15-0806).[49] In the XRD patterns of Mn/N–C, the peaks at $2\theta$ values of 34.9°, 40.5°, 58.7°, 70.2° and 73.8° were attributed to the characteristic peaks of MnO.[50] The addition of a low content of Mn improves the

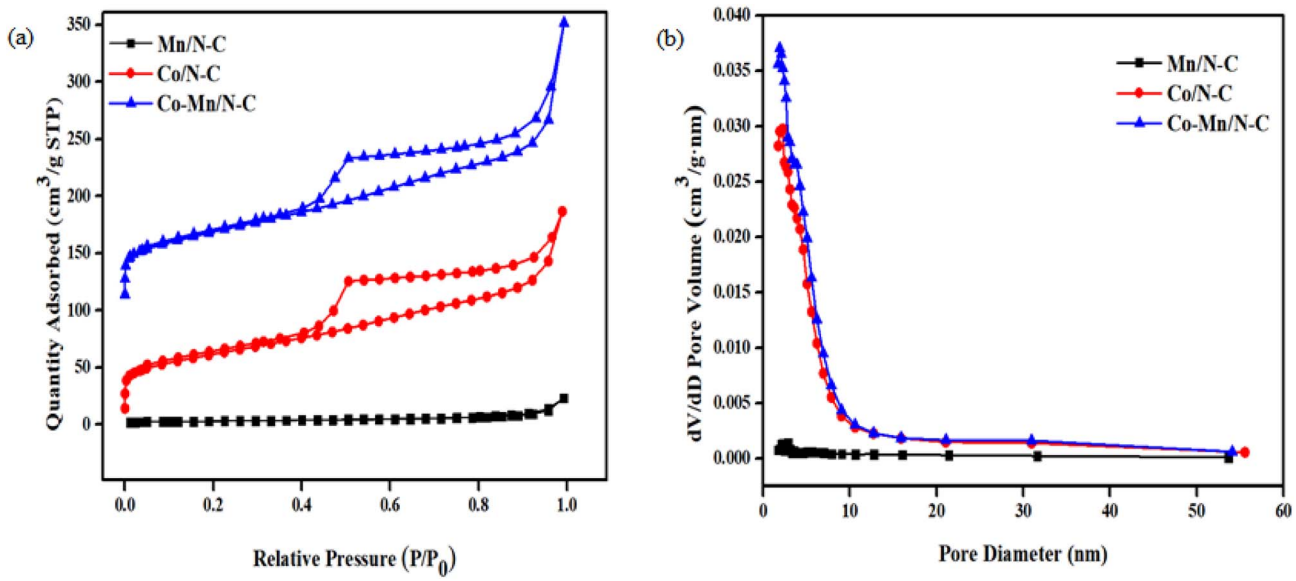


Fig. 5 $N_2$ adsorption–desorption isotherm (a) and pore size distribution curves (b) of Co–Mn/N–C, Co/N–C, and Mn/N–C.

Table 1 Surface area and pore volume of the Mn/N–C, Co/N–C and Co–Mn/N–C catalysts

| Entry | Catalyst | $S_{BET}$ ($m^2$ $g^{-1}$) | $V_p$ ($cm^3$ $g^{-1}$) | $S_p$ (nm) |
|---|---|---|---|---|
| 1 | Mn/N–C | 10.0 | 0.03 | 16.2 |
| 2 | Co/N–C | 239.1 | 0.36 | 7.7 |
| 3 | Co–Mn/N–C | 210.7 | 0.25 | 6.7 |

dispersion of the Co–Mn phase. It was noted that Mn species were not observed in the Co–Mn/N–C spectra due to the Mn elements being homogenously dispersed on the Co–Mn/N–C catalyst.

TEM analysis was employed to further investigate the morphology of the Co–Mn/N–C catalyst, as depicted in Fig. 2. As shown in Fig. 2a, the Co–Mn/N–C catalyst exhibits a rod-like structure. Many Co nanoparticles were randomly embedded in the carbon layer, as observed in Fig. 2b. Fig. 2d represents an

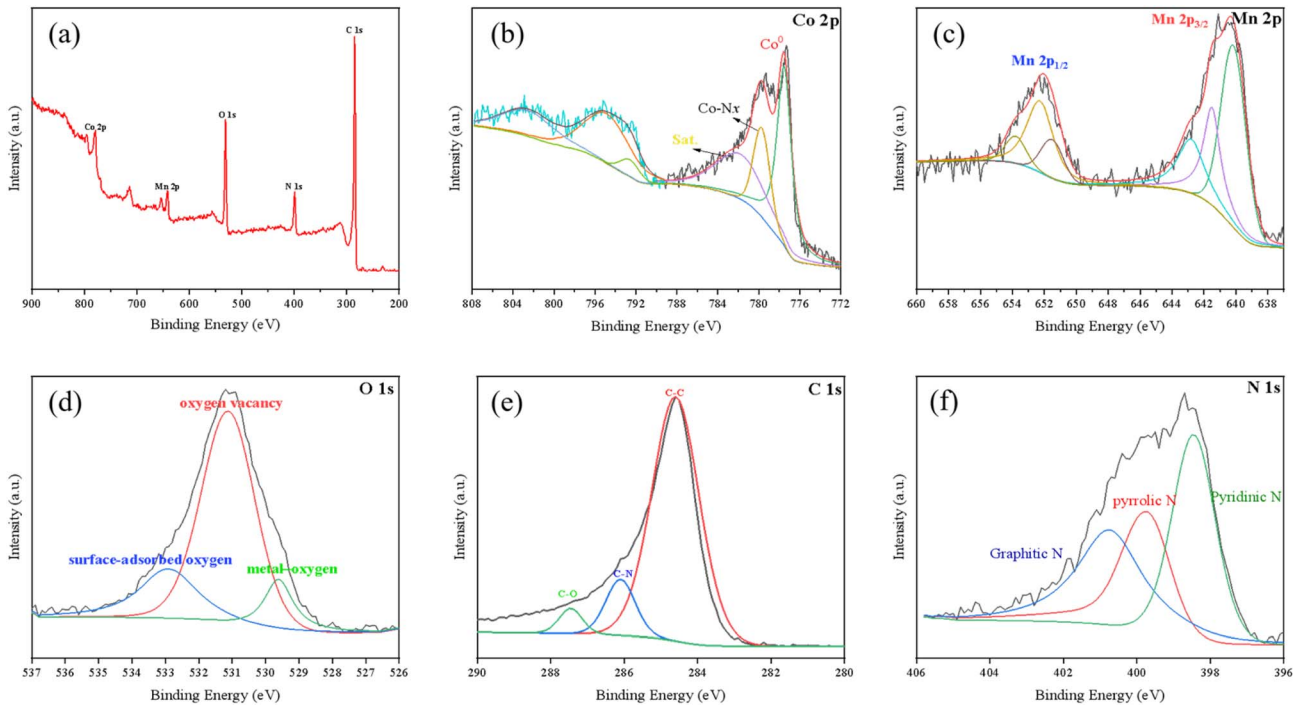


Fig. 6 XPS spectra for Co–Mn/N–C: (a) survey scan; (b) Co 2p; (c) Mn 2p; (d) O 1s; (e) C 1s; and (f) N 1s.

Table 2 Oxidation of HMF in the presence of various catalysts and bases in water[a]

| Entry | Catalyst | Base | HMF conv. (%) | Sel. (%) | | | |
|---|---|---|---|---|---|---|---|
| | | | | HFCA | FFCA | FDCA | Others |
| 1 | Mn/N–C | $Na_2CO_3$ | 62.8 | 25.0 | 56.5 | 0 | 18.5 |
| 2 | Co/N–C | $Na_2CO_3$ | 62.3 | 22.3 | 64.2 | 5.3 | 8.2 |
| 3 | Co–Mn/N–C | $Na_2CO_3$ | 78.0 | 20.0 | 69.4 | 9.5 | 1.1 |
| 4 | Co–Mn/N–C | None | 19.6 | 40.2 | 47.3 | 0 | 12.5 |
| 5 | Co–Mn/N–C | NaOH | 63.6 | 37.4 | 55.0 | 4.5 | 3.1 |
| 6 | Co–Mn/N–C | $NaHCO_3$ | 43.7 | 18.1 | 75.3 | 3.6 | 3.0 |

[a] Reaction conditions: 0.5 mmol HMF, 0.5 mmol base, 20 mg catalyst, 10 mL $H_2O$, 6 h, 100 °C, and 0.5 MPa $O_2$.

enlarged portion of Fig. 2c. The measured lattice spacing of 0.29 nm and 0.14 nm corresponds to the (002) crystal plane of graphite carbon and the (200) crystal plane of cobalt, respectively (Fig. 2d). The elemental distribution of Mn, Co, N, and C on the Co–Mn/N–C catalyst was investigated and visually represented using distinct colors, as depicted in Fig. 3a. As illustrated in Fig. 3b, some agglomeration of metallic Co was observed. This observation is consistent with the presence of diffraction peaks associated solely with metal Co in the XRD spectra. Both Mn and N elements exhibited a uniform distribution on the carbon support. This phenomenon may be attributed to the relatively low content of Mn. Furthermore, the strong coordination between Mn and N may effectively avoid the aggregation of Mn atoms, resulting in a homogeneous dispersion on the Co–Mn/N–C catalyst.[51]

The magnetic property of the Co–Mn/N–C catalyst was measured by a VSM at a magnetic field of ±1.5 T/MH at room temperature, and the results are shown in Fig. 4. From Fig. 4, the magnetic hysteresis curve the coercivity field ($H_c$) and saturation magnetization ($M_s$) values were 436.1 G and 15.4 emu per g, respectively. The results indicate that Co–Mn/N–C belongs to hard magnetic materials, suggesting that it can be used as a magnetic-supported catalyst.

The $N_2$ adsorption–desorption isotherms of Co/N–C, Mn/N–C, and Co–Mn/N–C were investigated. In Fig. 5a, $N_2$ adsorption isotherms of both Co/N–C and Co–Mn/N–C are type IV according to the IUPAC classification, indicating the existence of mesoporous structures. Moreover, $N_2$ adsorption isotherms of Co/N–C and Co–Mn/N–C did not show any adsorption limitation at high relative pressure, indicating a type $H_3$ hysteresis loop, which may be caused by the slit pores of the catalyst. Table 1 reveals that Mn/N–C exhibits the lowest specific surface area and pore volume (10.0 $m^2\ g^{-1}$ and 0.03 $cm^3\ g^{-1}$, respectively), whereas Co/N–C possesses significantly higher values (239.1 $m^2\ g^{-1}$ and 0.36 $cm^3\ g^{-1}$). The primary reason for the very low surface area and pore volume of Mn/N–C is likely due to the inability of manganese to facilitate the formation of a porous carbon framework during pyrolysis unlike cobalt. Notably, Co–Mn/N–C exhibits a larger specific surface area and pore volume, reaching 210.7 $m^2\ g^{-1}$ and 0.25 $cm^3\ g^{-1}$, respectively. A greater specific surface area and higher pore volume are advantageous for facilitating contact between the catalyst and reactants, thus enhancing the catalytic activity of the catalyst.[52]

XPS characterization was further performed to investigate the composition and valence states of elements. Elemental signals of C, N, O, Mn and Co are observed in the XPS survey spectrum of Co–Mn/N–C (Fig. 6a), whereas only C, N, O and Co are detected for Co/N–C (Fig. S3), and C, N, O and Mn for Mn/N–C (Fig. S4). The fitted peak at 778.3 eV observed in the high-resolution spectrum of Co $2p_{3/2}$ (Fig. 6b) indicates the presence of $Co^0$, while the peak at 779.6 eV corresponds to Co–$N_x$ with a pair of satellite peaks at 782.2 and 803.2 eV.[53] It is worth noting that the Co 2p binding energies of Co–Mn/N–C exhibit a slight shift compared with those of Co/N–C, attributable to the

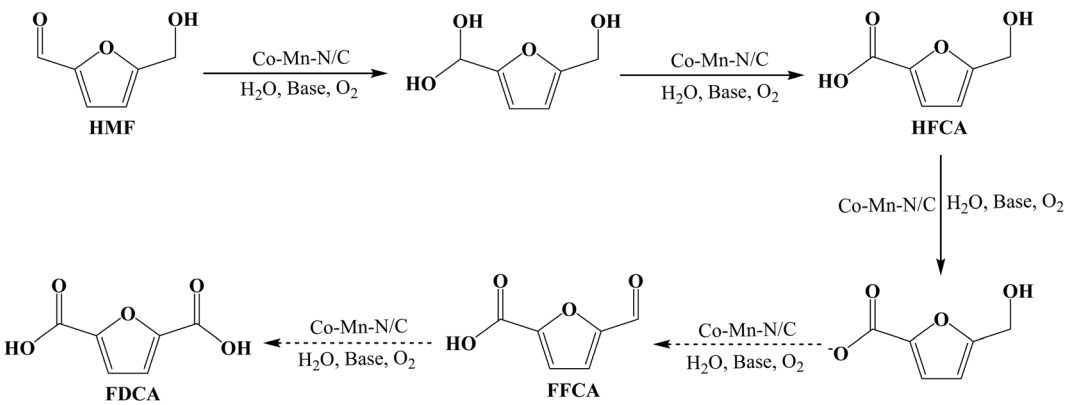


Scheme 3 Possible pathway for the HMF oxidation catalyzed by the Co–Mn/N–C catalyst.

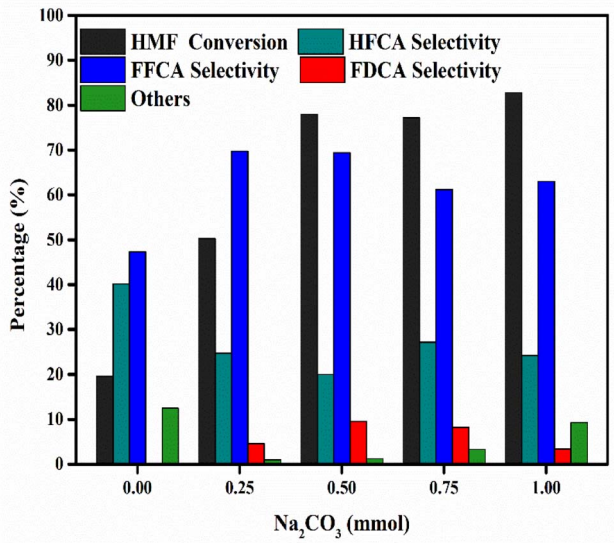


Fig. 7 Effects of the $Na_2CO_3$ amount on the HMF oxidation over Co–Mn/N–C in water. Reaction conditions: 0.5 mmol HMF, 100 °C, 20 mg Co–Mn/N–C, 10 mL $H_2O$, 6 h, and 0.5 MPa $O_2$.

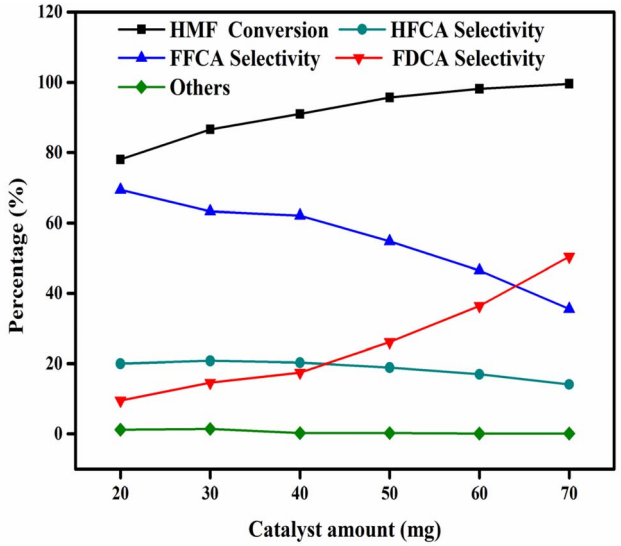


Fig. 8 Effects of the catalyst amount on the HMF oxidation in water. Reaction conditions: 0.5 mmol HMF, 0.5 mmol $Na_2CO_3$, 100 °C, 6 h, 10 mL $H_2O$, and 0.5 MPa $O_2$.

electronic-structure modulation induced by Mn introduction (Fig. S5). Fig. 6c shows the high-resolution spectra of Mn 2p in Co–Mn/N–C catalysts, and the Mn $2p_{3/2}$ peak at 641.3 eV is attributed to the Mn–$N_x$ moieties.[51] Similarly, the binding energy of Mn in Co–Mn/N–C differs from that in Mn/N–C due to the presence of Co (Fig. S6). The O 1s high-resolution spectra were further analyzed to explore the surface oxygen species (Fig. 6d). The peak at *ca.* 529.6 eV corresponds to lattice oxygen provided by metal–oxygen bonds. The peak at a binding energy of 531.1 eV is attributed to oxygen-related defects and consequent adsorbed oxygen, including free oxygen molecules, which act directly in catalytic reactions on the surfaces/interfaces of different metal elements and carbon. The peak at a binding energy of 532.8 eV indicates the presence of surface oxygen species with low reactivity. In the C 1s spectrum (Fig. 6e), the three peaks at the binding energies of 284.6, 286.1 and 287.4 eV belong to C–C, C–N and C–O bonds, respectively. The presence of the C–N bond in the catalyst implies the possibility of rapid electron transfer during the reaction, thereby enhancing the catalytic activity of the catalyst.[54] The high-resolution spectrum of N 1s (Fig. 6f) can be divided into three peaks corresponding to pyridinic N (398.4 eV), pyrrolic N (399.7 eV) and graphitic N (400.7 eV).[55] These results prove the successful integration of Mn and N into the carbon matrix.

### 3.2 Catalytic evaluation of the Co–Mn/N–C catalysts

As presented in Table 2, all the samples demonstrated good catalytic activity in the conversion of HMF, producing HFCA and FFCA as the main products. The monometallic Mn/N–C catalyst primarily facilitates the oxidation of the alcohol group, leading to high FFCA selectivity (Table 2, Entry 1). In contrast, the Co/N–C catalyst shows a greater tendency to activate molecular oxygen, promoting further oxidation toward FDCA (Table 2, Entry 2). Notably, the Co–Mn/N–C catalyst exhibits superior activity and FDCA selectivity (Table 2, Entry 3), likely due to a synergistic interaction between the Co and Mn sites that enhances oxygen activation and facilitates the sequential oxidation pathway from HMF to FDCA. 78.0% HMF conversion and 9.5% FDCA selectivity were achieved using $Na_2CO_3$ as the base, and the carbon balance of the reaction reached 99.3%. More importantly, the addition of a base was also crucial, as evidenced by the low conversion (19.6%) in its absence (Table 2, Entry 4). Different bases, such as NaOH and $NaHCO_3$, were further screened under the same reaction conditions. It was

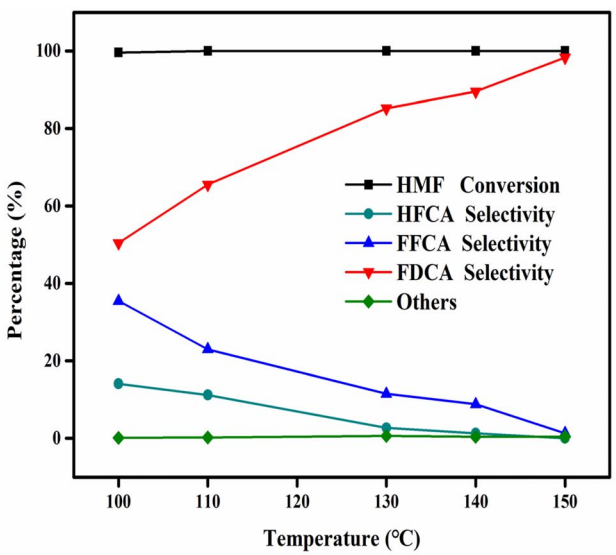


Fig. 9 Effects of temperature on HMF oxidation over Co–Mn/N–C in water. Reaction conditions: 0.5 mmol HMF, 0.5 mmol $Na_2CO_3$, 70 mg Co–Mn/N–C, 10 mL $H_2O$, 0.5 MPa $O_2$, and 6 h.

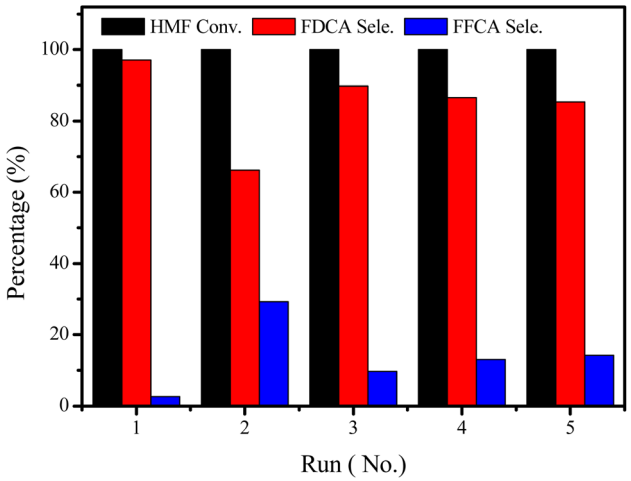


Fig. 10 Recyclability experiments of Co–Mn/N–C. Reaction conditions: 0.5 mmol HMF, 0.5 mmol $Na_2CO_3$, 70 mg Co–Mn/N–C, 10 mL $H_2O$, 0.5 MPa $O_2$, 6 h, and 150 °C.

observed that more FFCA and less FDCA were produced under strong alkaline conditions (Table 2, Entry 5). This suggests that strong alkalinity efficiently promotes the oxidation of the alcohol group to form FFCA, but may inhibit the final step of FFCA oxidation to FDCA potentially due to excessive deprotonation of the reaction intermediates or catalyst surface. However, the conversion of HMF decreased significantly when the weaker base, $NaHCO_3$ was added (Table 2, Entry 6). Therefore, $Na_2CO_3$ as a suitable base was further investigated for the oxidation of HMF over the Co–Mn/N–C catalyst. The by-product DFF was not detected in the reaction solutions for any of the three catalysts, underscoring that the oxidation of HMF predominantly proceeds *via* the aldehyde group pathway (HMF → HFCA → FFCA → FDCA). The possible reaction pathway for HMF oxidation is proposed, as shown in Scheme 3. Notably, FFCA accumulates with high selectivity, which indicates that the oxidation step (FFCA → FDCA) is rate-limiting. Based on these findings, Co–Mn/N–C was selected for further investigation.

The effect of $Na_2CO_3$ amount on HMF oxidation was also studied, and the results are shown in Fig. 7. The HMF conversion increased with the increase in the amount of $Na_2CO_3$, up to 0.5 mmol. It was clearly observed that the presence of $Na_2CO_3$ can facilitate the oxidation reaction of HMF, which probably increases the pH of the solution, thus favoring the oxidation of the aldehyde groups of HMF.[56] However, with a further increase in the amount of $Na_2CO_3$, the FDCA selectivity decreased, which could be explained by the generation of by-products such as other furan-based intermediates and/or humins in the reaction mixture.

The effect of Co–Mn/N–C dosage on HMF oxidation was studied. In Fig. 8, as expected, the conversion of HMF exhibits a gradual increase with the increase in the catalyst amount. Upon incrementing the catalyst dosage from 20 mg to 70 mg, a discernible decrease in the selectivity of the intermediate products, 5-hydroxymethyl-2-furancarboxylic acid (HFCA) and 5-formyl-2-furancarboxylic acid (FFCA), was observed. The selectivity for 2,5-furandicarboxylic acid (FDCA) exhibited a consistent and progressive enhancement. At a catalyst dosage of 70 mg, the conversion of HMF and the selectivity towards FDCA reached a maximum of 99.6% and 50.4%, respectively. Based on the above results, a catalyst dosage of 70 mg was opted for subsequent experimental studies.

The effect of temperature on HMF oxidation was investigated between 100 and 150 °C, and the results are displayed in Fig. 9. It was observed that complete conversion of HMF was achieved at 110 °C. In addition, the selectivity for 2,5-furandicarboxylic acid (FDCA) increased considerably with rising temperature, giving 98.3% selectivity for FDCA at 150 °C. Furthermore, during the reaction process, the intermediate products HFCA

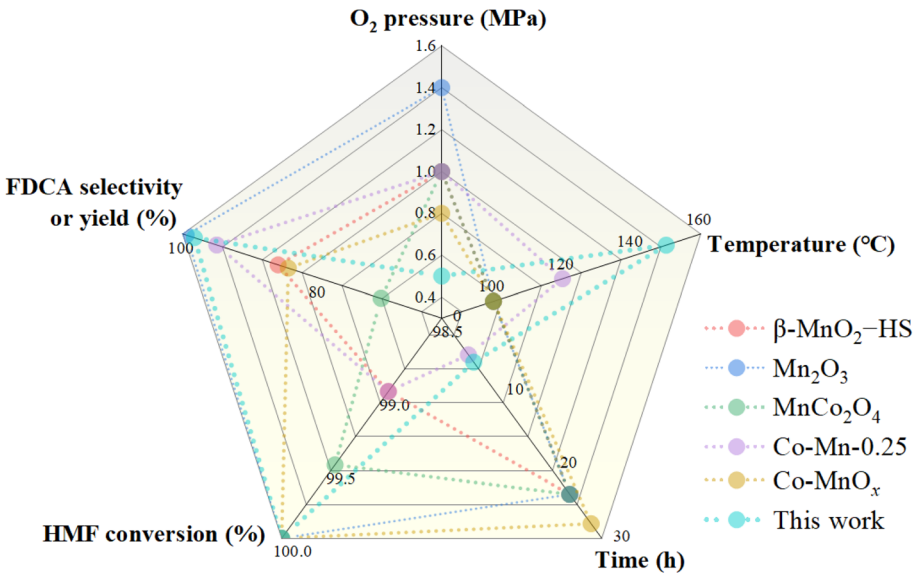


Fig. 11 Comparison of various catalysts for the selective oxidation of HMF to FDCA.

and FFCA were detected, whereas the by-product DFF was not detected. Meanwhile, the detected intermediate products, FFCA and HFCA, decreased with increasing temperature. This phenomenon can be explained by the further oxidation of both FFCA and HFCA to FDCA at high reaction temperatures.

The recyclability of the catalyst is very important for HMF oxidation in water. The Co–Mn/N–C catalyst can be easily separated using magnets after each use owing to the magnetic properties of the catalyst. As presented in Fig. 10, the selectivity of FDCA decreased from 97.1% to 66.2% after the first use. The ICP-OES analysis showed that no Co or Mn element was detected in the solution after the reaction, indicating that the Co and Mn elements on the catalyst were stable. The used catalyst was further characterized by XRD to compare with the fresh catalyst, and a new diffraction peak at 36.8°, which belonged to $Co_3O_4$, was observed (Fig. S7), which may lead to a decrease in the catalyst activity. Therefore, the catalyst was calcined in a $H_2$ atmosphere before the next use. Notably, the catalytic activity of Co–Mn/N–C could be partly restored, giving relatively acceptable selectivity towards FDCA.

The catalytic performances of various catalysts for the selective oxidation of HMF to FDCA were further compared using $O_2$ as an oxidant in an aqueous medium. As shown in Fig. 11, manganese dioxides with different crystal structures, such as β-$MnO_2$-HS[57] and $Mn_2O_3$ nanoflakes,[58] show high activity for the aerobic oxidation of HMF. Moreover, bimetals of Co and Mn, such as $MnCo_2O_4$,[59] Co–Mn-0.25 (ref. 60) and Co-$MnO_x$,[61] can be rationally designed and prepared and exhibit high effectiveness for the oxidation of HMF into FDCA. It can be found that the Co–Mn/N–C catalyst exhibits a relatively high HMF conversion and satisfactory FDCA selectivity under mild conditions.

## 4 Conclusion

A novel rod-like magnetic catalyst, Co–Mn/N–C, was obtained using citric acid, melamine, manganese sulfate, and cobalt chloride as precursors through a calcination process at 700 °C. Co–Mn/N–C catalyst shows excellent catalytic performance for the oxidation of HMF into FDCA in water. Under optimal reaction conditions, HMF could be completely converted and the selectivity of FDCA could reach as high as 98.3%. Additionally, the magnetic properties of the catalyst facilitated easy separation from the catalytic system. This study provides a significant and challenging effort in the utilization of non-noble metal catalysts supported on N–C materials for the conversion of HMF into FDCA using molecular oxygen as the oxidant.

## Author contributions

Shuolin Zhou: investigation, visualization, writing – reviewing and editing, project administration, funding acquisition. Wen Sha: investigation, data curation, formal analysis, visualization. Ying Liu: investigation, visualization. Xianxiang Liu: conceptualization, methodology, project administration, funding acquisition, supervision.

## Conflicts of interest

The authors declare that they have no known competing financial interests or personal relationships that could have appeared to influence the work reported in this paper.

## Data availability

Data supporting this article have been included as part of the supplementary information (SI) with the original data available from the corresponding authors on request. Supplementary information: details of the HPLC results, $^1$H NMR analysis, XPS and XRD. See DOI: https://doi.org/10.1039/d5su00783f.

## Acknowledgements

This work was supported by the National Natural Science Foundation of China (Grant No. 22278121), the Hunan Provincial Natural Science Foundation of China (Grant No. 2026JJ81172 and 2026JJ50394), and the Scientific Research Fund of the Hunan Provincial Education Department (Grant No. 22B1095).

## References

1 P. A. Østergaard, N. Duic, Y. Noorollahi and S. Kalogirou, *Renewable Energy*, 2022, **199**, 1145–1152.
2 S. Biswas, B. Dutta, A. Mannodi-Kanakkithodi, R. Clarke, W. Song, R. Ramprasad and S. L. Suib, *Chem. Commun.*, 2017, **53**, 11751–11754.
3 J. Nie and H. Liu, *Pure Appl. Chem.*, 2011, **84**, 765–777.
4 R. Fang, R. Luque and Y. Li, *Green Chem.*, 2016, **18**, 3152–3157.
5 R. Mori, *RSC Sustain.*, 2023, **1**, 179–212.
6 F. Brienza, D. Cannella, D. Montesdeoca, I. Cybulska and D. P. Debecker, *RSC Sustain.*, 2024, **2**, 37–90.
7 A. He, Q. Gu, X. Shen, J. Zheng, L. Hu, X. Wang, Y. Jiang, Z. Wu, J. Xu and J. Song, *Green Chem.*, 2023, **25**, 2349–2360.
8 L. G. Tonutti, B. O. Dalla Costa, G. Mendow, G. L. Pestana, N. S. Veizaga and J. M. Grau, *Micropor. Mesopor. Mater.*, 2022, **343**, 112145.
9 W. Zhao, X. Zhu, Z. Zeng, J. Lei, Z. Huang, Q. Xu, X. Liu and Y. Yang, *Mol. Catal.*, 2022, **524**, 112304.
10 Z. Huang, Z. Zeng, X. Zhu, W. Zhao, J. Lei, Q. Xu, Y. Yang and X. Liu, *Front. Chem. Sci. Eng.*, 2023, **17**, 415–424.
11 W. Zhao, Z. Huang, L. Yang, X. Liu, H. Xie and Z. Liu, *Appl. Surf. Sci.*, 2022, **577**, 151869.
12 R. Guo, Y. Zeng, L. Lin, D. Hu, C. Lu, S. Conroy, S. Zhang, C. Zeng, H. Luo, Z. Jiang, X. Zhang, X. Tu and K. Yan, *Angew. Chem., Int. Ed.*, 2025, **64**, e202418234.
13 C. A. Antonyraj, N. T. T. Huynh, K. W. Lee, Y. J. Kim, S. Shin, J. S. Shin and J. K. Cho, *J. Chem. Sci.*, 2018, **130**, 156.
14 T. K. T. Le, S. Kongparakul, H. Zhang, J. Zhao, G. Guan, N. Chanlek, T. T. V. Tran and C. Samart, *Mol. Catal.*, 2023, **539**, 113017.
15 C. A. Celaya, R. Oukhrib, M. A. El Had, Y. Abdellaoui, H. A. Oualid, H. Bourzi, R. Chahboun, D. Zhao,

S. M. Osman, V. S. Parmar and C. Len, *Mol. Catal.*, 2022, **519**, 112117.
16 J. Lai, F. Cheng, S. Zhou, S. Wen, D. Guo, W. Zhao, X. Liu and D. Yin, *Appl. Surf. Sci.*, 2021, **565**, 150479.
17 X. Liu, J. Xiao, H. Ding, W. Zhong, Q. Xu, S. Su and D. Yin, *Chem. Eng. J.*, 2016, **283**, 1315–1321.
18 J. Lai, S. Zhou, F. Cheng, D. Guo, X. Liu, Q. Xu and D. Yin, *Catal. Lett.*, 2020, **150**, 1301–1308.
19 J. Han, M. Song, Y. Li, Y. Yao, S. Lu and X. Liao, *React. Chem. Eng.*, 2024, **9**, 148–159.
20 J. Li, G. Wang, X. Wang, Y. Zhao, Y. Zhao, W. Sui, D. Wang and C. Si, *ACS Catal.*, 2024, **14**, 16003–16013.
21 K. Zhao, B. Wen, Q. Tang, F. Wang, X. Liu, Q. Xu and D. Yin, *Green Chem.*, 2024, **26**, 9957–9992.
22 Z. Zheng, K. Li, L. Lin, Z. Jiang, Y. Wang and K. Yan, *Green Energy Environ.*, 2025, **10**, 898–916.
23 H. Zhang, Z. Feng, Y. Zhu, Y. Wu and T. Wu, *J. Photochem. Photobio. A: Chem.*, 2019, **371**, 1–9.
24 C. Chang, X. Ma and P. Cen, *Chin. J. Chem. Eng.*, 2006, **14**, 708–712.
25 M. Ventura, M. Aresta and A. Dibenedetto, *ChemSusChem*, 2016, **9**, 1096–1100.
26 P. Pan, M. Li, Y. Liu, Y. Feng and X. Li, *Mol. Catal.*, 2022, **530**, 112622.
27 Z. Zeng, L. Yang, X. Zhu, W. Zhao, X. Liu, Z. Huang, Q. Xu and W. Zhong, *React. Chem. Eng.*, 2023, **8**, 455–464.
28 B. S. Solanki and C. V. Rode, *J. Saudi Chem. Soc.*, 2019, **23**, 439–451.
29 H. Zhou, H. Xu, X. Wang and Y. Liu, *Green Chem.*, 2019, **21**, 2923–2927.
30 L. Gao, K. Deng, J. Zheng, B. Liu and Z. Zhang, *Chem. Eng. J.*, 2015, **270**, 444–449.
31 M. Sajid, X. Zhao and D. Liu, *Green Chem.*, 2018, **20**, 5427–5453.
32 G. Totaro, L. Sisti, P. Marchese, M. Colonna, A. Romano, C. Gioia, M. Vannini and A. Celli, *ChemSusChem*, 2022, **15**, e202200501.
33 D. Zhao, T. Su, Y. Wang, R. S. Varma and C. Len, *Mol. Catal.*, 2020, **495**, 111133.
34 C. Chen, L. Wang, B. Zhu, Z. Zhou, S. I. El-Hout, J. Yang and J. Zhang, *J. Energy Chem.*, 2021, **54**, 528–554.
35 E. Hayashi, T. Komanoya, K. Kamata and M. Hara, *ChemSusChem*, 2017, **10**, 654–658.
36 F. Cheng, D. Guo, J. Lai, M. Long, W. Zhao, X. Liu and D. Yin, *Front. Chem. Sci. Eng.*, 2021, **15**, 960–968.
37 F. Wang, J. Lai, Z. Liu, S. Wen and X. Liu, *Biomass Convers. Bior.*, 2023, **13**, 16887–16898.
38 T. Gao, Y. Yin, G. Zhu, Q. Cao and W. Fang, *Catal. Today*, 2020, **355**, 252–262.
39 E. Hayashi, Y. Yamaguchi, K. Kamata, N. Tsunoda, Y. Kumagai, F. Oba and M. Hara, *J. Am. Chem.Soc.*, 2019, **141**, 890–900.
40 S. Chen, Y. Cheng, H. Ban, Y. Zhang, L. Zheng, L. Wang and X. Li, *Ind. Eng. Chem. Res.*, 2020, **59**, 17076–17084.
41 X. Han, C. Li, X. Liu, Q. Xia and Y. Wang, *Green Chem.*, 2017, **19**, 996–1004.
42 H.-z. Lu, J.-f. Bai, F. Yan, X.-y. Zhang, Y. Jin, J.-y. Wang, P. Chen and M.-d. Zhou, *J. Fuel Chem. Technol.*, 2021, **49**, 312–321.
43 F. Yang, Y. Ding, J. Tang, S. Zhou, B. Wang and Y. Kong, *Mol. Catal.*, 2017, **435**, 144–155.
44 C. Chen, L. Wang, B. Zhu, Z. Zhou, S. I. El-Hout, J. Yang and J. Zhang, *J. Energy Chem.*, 2021, **54**, 528–554.
45 L. Yang, J. Liu, F. Cheng, S. Zhou, Q. Xu, D. Yin and X. Liu, *Renewable Energy*, 2024, **226**, 120409.
46 F. Wang, J. Lai, Z. Liu, S. Wen and X. Liu, *Biomass Convers. Bior.*, 2023, **13**, 16887–16898.
47 Z. Zeng, Q. Tang, B. Wen, L. Luo, X. Liu, Q. Xu, W. Zhong and J. Enviorn, *Chem. Eng.*, 2024, **12**, 112190.
48 S. K. Singh, M. J. Akhtar and K. K. Kar, *Ind. Eng. Chem. Res.*, 2020, **59**, 9076–9084.
49 Y. Chen, M. Lu, J.-E. Zhou, X. Zhang, Y. Li, X. Lin, A. Zeb and Z. Xu, *Electrochim. Acta*, 2022, **435**, 141355.
50 K. Hou, T. Wang, X. Jing and L. Zhang, *Mater. Chem. Phys.*, 2023, **303**, 127744.
51 H. Zhou, H. Xu and Y. Liu, *Appl. Catal. B: Environ.*, 2019, **244**, 965–973.
52 Y. Wang, H. Arandiyan, J. Scott, A. Bagheri, H. Dai and R. Amal, *J. Mater. Chem. A*, 2017, **5**, 8825–8846.
53 T. Jing, S. Yang, Y. Feng, T. Li, Y. Zuo and D. Rao, *Nano Res.*, 2023, **16**, 6670–6678.
54 R. Kumar, Z. Zhu, C. Chen, W. Cai, J. Woon-Chung Wong and J. Zhao, *ChemSusChem*, 2022, **15**, e202201333.
55 J. Yu, Q. Zhou, X. Xue, H. Zhang, X. Li, F. Wang, Q. Chen and H. Zhu, *New J. Chem.*, 2021, **45**, 14608–14615.
56 L. Zhang, X. Luo and Y. Li, *J. Energy Chem.*, 2018, **27**, 243–249.
57 E. Hayashi, Y. Yamaguchi, K. Kamata, N. Tsunoda, Y. Kumagai, F. Oba and M. Hara, *J. Am. Chem. Soc.*, 2019, **141**, 890–900.
58 L. Bao, F.-Z. Sun, G.-Y. Zhang and T.-L. Hu, *ChemSusChem*, 2020, **13**, 548–555.
59 S. Zhang, X. Sun, Z. Zheng and L. Zhang, *Catal. Commun.*, 2018, **113**, 19–22.
60 K. T. V. Rao, J. L. Rogers, S. Souzanchi, L. Dessbesell, M. B. Ray and C. Xu, *ChemSusChem*, 2018, **11**, 3323–3334.
61 K. Yu, Y. Liu, D. Lei, Y. Jiang, Y. Wang, Y. Feng, L.-L. Lou, S. Liu and W. Zhou, *Catal. Sci. Techol.*, 2018, **8**, 2299–2303.